Acta Materialia 126 (2017) 552–563

Contents lists available at ScienceDirect

Acta Materialia

journal homepage: www.elsevier.com/locate/actamat

Full length article

Misfit dislocation patterns of Mg-Nb interfaces

Y. Chen [a], S. Shao [b], X.-Y. Liu [c], S.K. Yadav [c], N. Li [a], N. Mara [a, d], J. Wang [e, *]

[a] MPA-CINT, Los Alamos National Laboratory, Los Alamos, NM, 87545, USA
[b] Department of Mechanical and Industrial Engineering, Louisiana State University, Baton Rouge, LA, 70803, USA
[c] MST-8, Los Alamos National Laboratory, Los Alamos, NM, 87545, USA
[d] Institute for Materials Science (IMS), Los Alamos National Laboratory, Los Alamos, NM 87545, USA
[e] Mechanical and Materials Engineering, University of Nebraska-Lincoln, Lincoln, NE, 68588, USA

ARTICLE INFO

Article history:
Received 7 September 2016
Received in revised form
22 November 2016
Accepted 16 December 2016
Available online 20 January 2017

Keywords:
Hcp/bcc interface
Bimetal interface
Layered nanocomposite
Atomically informed Frank-Bilby

ABSTRACT

The role of heterogeneous interfaces in improving mechanical properties of polycrystalline aggregates and laminated composites has been well recognized with interface structure being of fundamental importance in designing composites containing multiple interfaces. In this paper, taking the Mg (hexagonal close-packed (hcp))/Nb (body-centered cubic (bcc)) interface as an example, we develop Mg-Nb interatomic potentials for predicting atomic configurations of Mg/Nb interfaces. We systematically characterize interface dislocations of Mg/Nb interfaces with Nishiyama-Wassermann (NW) and Kurdjumov-Sachs (KS) orientation relationships and propose a generalized procedure of characterizing interface structure by combining atomistic simulation and interface dislocation theory, which is applicable for not only hcp/bcc interfaces, but also other systems with complicated interface dislocation configurations. In Mg/Nb, interface dislocation networks of two types of interfaces are significantly different although they originate from partial dislocations of similar character: the NW interface is composed of three sets of partial dislocations, while the KS interface is composed of four sets of interface dislocations - three sets of partial dislocations and one set of full dislocations that forms from the reaction of two close partial dislocations.

1. Introduction

Magnesium (Mg) and its alloys, benefiting from the lowest weight/volume ratio among all metals have a huge potential in the aerospace and automotive industries [1,2]. However, Mg and Mg alloys have low ductility and poor formability at room temperature due to scarcity of easy slip systems and the propensity for localized shear via twinning in hexagonal close-packed (hcp) structures [3–6]. Many techniques, such as non-traditional processing [7,8], grain refinement [9–11], nano-spaced stacking faults [12], and alloying with rare earth elements [13–15] etc., have been applied to tune the relative activity of slip and twinning in Mg and Mg alloys, improving deformability while maintaining high flow strength. Other than these, Mg and Mg alloys can be strengthened through tailoring microstructure of Mg-based composites, such as Mg-metal laminates [16,17].

Metallic layered composites containing a high density of interfaces show promising enhancement in both strength and ductility [18]. Lu et al. [17] demonstrated that the mechanical strength of Mg/Ti multilayers could achieve a high value of ~1.5 GPa when the layers are a few nanometers thick. In Mg/Nb, Ham and Zhang [16] found that the mechanical strength of the Mg/Nb multilayers is ~1.0 GPa. Using transmission electron microscopy (TEM), we have explored that Mg can adopt different crystal structures in layered composites: a hexagonal close-packed structure (hcp-Mg) when the layer thickness of Mg is larger than ~5 nm and a body-centered cubic structure (bcc-Mg) when the layer thickness is less than ~5 nm. At small layer thickness, the existence of bcc-Mg layers is ascribed to the lower interface energy of the coherent bcc-Mg/Nb interface (303.7 mJ/m^2) compared to coherent and semi-coherent hcp-Mg/Nb interfaces (373 mJ/m^2 and 624 mJ/m^2) [19]. At large layer thickness, the formation of hcp-Mg in thick Mg layers is attributed to the higher bulk energy of bcc-Mg than hcp-Mg [19].

The strength of Mg-metal multilayers reported in the literature above is much greater than that of the majority of Mg alloys reported to date. Along with the improved mechanical properties under various types of mechanical testing [18,20–22], the influence of interface structure on mechanical behaviors has been reviewed

* Corresponding author.
E-mail address: jianwang@unl.edu (J. Wang).

http://dx.doi.org/10.1016/j.actamat.2016.12.041
1359-6454/

[23–28], including that of interface shearing [29,30], interfacial dislocation nucleation [31–35], gliding dislocation-interface interaction [36–38], interfacial dislocation climb [39,40] and interfacially-driven twinning [41–46]. To understand the role of Mg-metal interfaces in strengthening as well as plastic deformation, including nucleation and emission of dislocations and twinning from bimaterial interfaces, it is essential to quantitatively characterize the interface structures of Mg-metal multilayers. It is worth mentioning that the misfit dislocation structures that prevail at hcp related layer interfaces have not been investigated in detail and the methodology of identifying such structures is intrinsically linked to mechanical performance of hcp-based nanocomposites. In this paper, we adopt Mg/Nb as a model system to identify interface structure. We first identify the orientation relationships (ORs) of Mg/Nb multilayers by TEM and then we simulate hcp-Mg/Nb interfaces with the empirical interatomic potentials and analyze the dislocation structures of hcp-Mg/Nb interfaces.

Mg/Nb multilayers with individual layer thickness of 50 nm were prepared by magnetron sputtering. Cross-sectional TEM analysis shows that hcp-Mg/Nb multilayers adopt (0001)||{110} interfaces (Fig. 1). Selected area diffraction (SAD) patterns of Mg/Nb multilayers indicate two ORs between hcp-Mg and Nb layers: (0001)||(01$\bar{1}$)||interface with <2$\bar{1}\bar{1}$ 0>||<111> and (0001)||(01$\bar{1}$)|| interface with <2$\bar{1}\bar{1}$ 0>||<100>. From a crystallographic viewpoint, <2$\bar{1}\bar{1}$ 0> in hcp structure is equivalent to <110> in face-centered cubic (fcc) structure and (0001) plane is equivalent to (111) in fcc structure. We refer the first OR to the Kurdjumov-Sachs (KS) OR and the second to the Nishiyama-Wassermann (NW) OR in terms of the KS and NW ORs in fcc/bcc systems.

KS and NW interface structures in fcc/bcc systems, such as Cu/Nb multilayers, have been systematically investigated [47,48]. Atomic planes around the interface have a stacking sequence … ABCABC|ABAB …, where the symbol "|" indicates the position of the interface plane. ABCABC ahead of "|" shows the stacking sequence of close-packed (111) planes in a fcc structure, and ABAB after "|" shows the stacking sequence of close-packed (110) planes in a bcc structure. We note that the first (110) plane in the bcc structure stacks in the normal stacking sequence of (111) planes to achieve a low-energy configuration. When replacing the fcc structure with an hcp structure to form a hcp/bcc interface, the stacking sequence near the hcp/bcc interface is no longer unique. Since hcp {0001} planes are stacking with a sequence … ABAB …, the hcp/bcc system could possibly have two stacking sequences of atomic planes around the interface, either … ABAB|CACA … or … ABAB|ABAB …, where ABAB ahead of "|" is the stacking sequence of (0001) planes in a hcp structure. In the former case CACA after "|" shows the stacking sequence of (110) planes in a bcc structure. The first (110) plane from the interface occupies a C-plane in terms of ABC stacking in a fcc structure. The interface is thus referred as a normal fcc structure (FCC). In the latter case, ABAB after "|" exhibits the stacking sequence of (110) planes in a bcc structure, the first (110) plane from the interface occupies the A-plane in terms of ABC stacking in a fcc structure, forming a stacking faulted structure at interface. The interface is thus referred as a stacking faulted structure (SF).

To analyze the misfit dislocation structures of hcp-Mg/Nb interfaces with KS and NW ORs, we first calculated the generalized stacking fault interface energy of coherent hcp/bcc interfaces and found two low-energy coherent interfaces, …ABAB|CACA … (FCC) and … ABAB|ABAB … (SF). The two coherent interfaces can interchange from one to the other by interface shear associated with interface dislocations. Secondly, we characterized misfit dislocation patterns of the KS and NW interfaces by atomically informed Frank-Bilby (AIFB) theory [47–49]. We found that both interfaces are

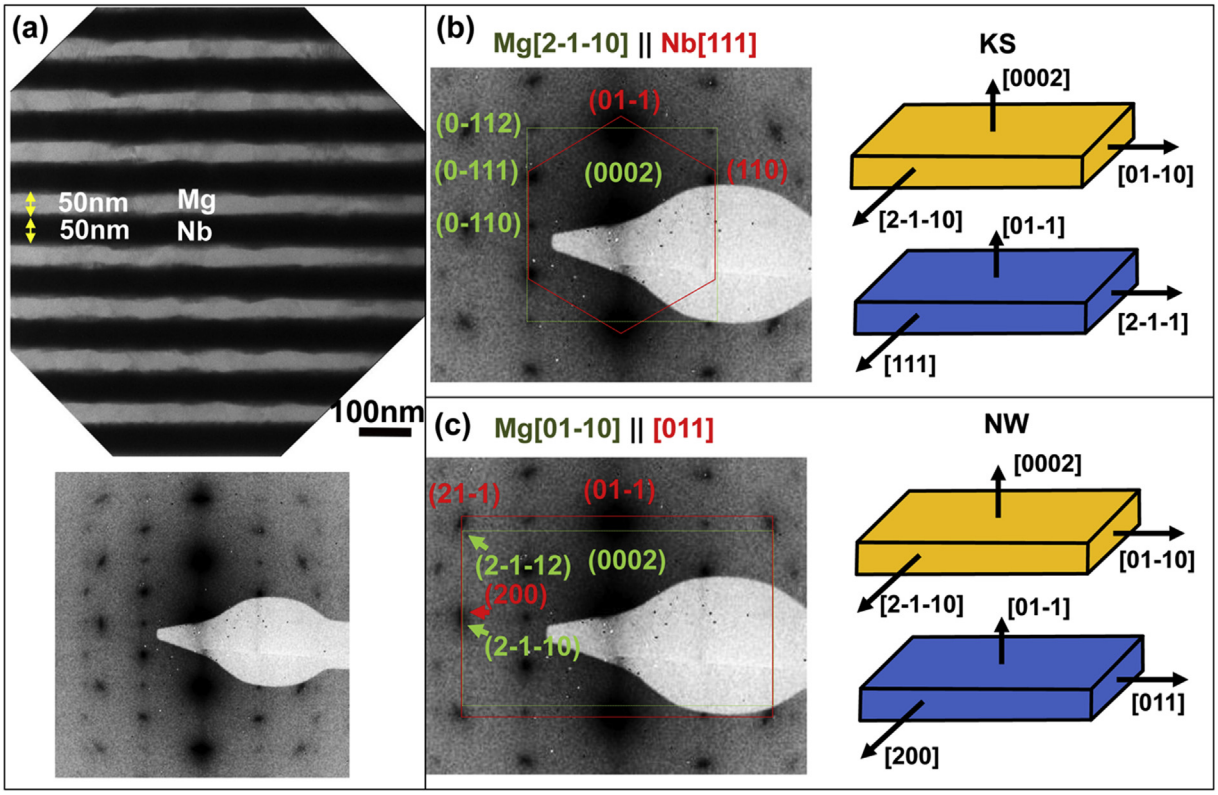

Fig. 1. (a) Cross-sectional transmission electron microscopy (TEM) micrograph and selected area diffraction (SAD) pattern of Mg/Nb multilayers with individual layer thickness of 50 nm. The SAD patterns indicate two orientation relationships between Mg and Nb: (b) KS OR and (c) NW OR.

initially composed of two coherent structures (FCC and SF) and three sets of partial dislocations, which is similar to that found in fcc/fcc interfaces, but that for the KS case of Mg/Nb, two sets of partial dislocations in close proximity to one another react to form full dislocations, increasing the complexity of characterizing these interface dislocations.

Correspondingly, this article is organized as follows. We describe essential details of atomistic simulations and interface characterization techniques in Section 2. In Section 3, we define reference lattices (commensurate/coherent dichromatic pattern (CDP) or Rotated CDP (RCDP)) [47–49] for Mg/Nb interfaces and possible Burgers vectors in the two lattices. Afterwards, we characterize misfit dislocations of Mg/Nb interfaces by using AIFB theory. We conclude that both NW and KS Mg/Nb interfaces originally are comprised of two types of coherent interfaces separated by three sets of partial dislocations, whereas two sets of near-parallel partial dislocations in KS interface react, forming four sets of interface dislocations. Finally, we generalize procedures of characterizing interface dislocation structures.

2. Interface characterization techniques

2.1. Mg-Nb interatomic potential

The embedded atom method (EAM) [50] was used to model bulk Mg [51], Nb [52], and the interaction between Mg and Nb. The development of cross potentials between Mg and Nb is accomplished by the following procedure as proposed by Demkowitcz et al. [53]. The interaction between Mg and Nb is described by a two-body Morse potential,

$$\phi_{MgNb}(r) = D_M\left(1 - e^{\alpha_M(r-R_M)}\right)^2 - D_M \tag{1}$$

where r is the distance, D_M, α_M and R_M are three fitting constants. To obtain a smooth curve at the cutoff radius r_{cut}, the potential function is modified to ensure that both the potential value and its first derivative are smoothly approaching zero at r_{cut},

$$\phi^{new}_{MgNb}(r) = \phi_{MgNb}(r) - \phi_{MgNb}(r_{cut}) + \frac{r_{cut}}{20}\left(1 - \frac{r^{20}}{r^{20}_{cut}}\right)\frac{d\phi_{MgNb}}{dr}\bigg|_{r=r_{cut}} \tag{2}$$

In addition, two transformation invariants were taken into consideration,

$$\begin{aligned} F^{new}(\bar{\rho}) &= F(\bar{\rho}) + g\bar{\rho}, \\ \phi^{new}(r) &= \phi(r) - 2g\rho(r) \end{aligned} \tag{3}$$

and

$$\begin{aligned} \rho^{new}(r) &= s\rho(r), \\ F^{new}(\bar{\rho}) &= F(\bar{\rho}/s) \end{aligned} \tag{4}$$

which adds three more fitting constants, g_{Mg}, g_{Nb}, and s_{Nb}.

Due to the immiscible nature of Mg-Nb systems, there is no equilibrium compound which can be used for fitting the cross potential. The lattice constant and bulk modulus of a hypothetical B2 (CsCl) phase MgNb obtained from first-principles density functional theory (DFT) calculations were used in fitting the cross potential. In addition, the dilute heats of mixing (Nb in Mg, and Mg in Nb) calculated from DFT were fitted.

The DFT calculations were performed using the Vienna *Ab initio* Simulation Package (VASP) [54,55]. The DFT calculations employed the Perdew, Burke, and Ernzerhof (PBE) [56] generalized gradient approximation (GGA) exchange-correlation functional and the projector-augmented wave (PAW) method [57]. For all calculations, a plane wave cutoff of 400 eV for the plane wave expansion of the wave functions was used. 15 × 15 × 15 Monkhorst-pack mesh for k-point sampling was used to obtain a well-converged bulk modulus and lattice parameter of B2 type MgNb, using a primitive unit cell. For dilute heats of mixing calculations, supercells of 48 atoms hcp Mg and 54 atoms bcc Nb were used, using Monkhorst-pack mesh for k-point sampling of 10 × 10 × 10. Force tolerance for the structural relaxation was 0.02 eV/Å. Table 1 lists the fitted properties of the newly constructed cross potentials for the Mg-Nb systems, and the fitted parameters for the cross-pair potential for the Mg-Nb system.

2.2. Molecular dynamics simulations of Mg/Nb interfaces

The relaxed, equilibrium interface structures are obtained by atomistic simulations with the empirical interatomic potentials for Mg, Nb, and Mg-Nb. Fig. 2a shows schematics of Mg/Nb bicrystal models. The interface plane is the x-z plane. Periodic boundary conditions are applied in both the x- and z-directions. The x and z dimensions with respect to the orientation relationship are determined due to the incommensurate nature of two crystals. The y-dimension for each crystal is 10 nm. A semi-rigid boundary with a fixed region of 2 nm from surfaces is applied in the y-direction to mimic the response of the bulk material.

For the NW interface, the x-axis is along $[\bar{1}100]$ for Mg and [110] for Nb, and the z-axis is along $[\bar{1}\bar{1}20]$ and [001]. The final dimensions of the bicrystal model are 8.876 nm and 9.920 nm in the x and z directions, corresponding to a super boundary unit cell at equilibrium. It contains 16 periodic units for Mg and 19 periodic units for Nb in the x-direction, and 31 periodic units for Mg and 30 periodic units for Nb in the z-direction. For the KS interfaces, the x-axis is along $[\bar{1}100]$ and $[2\bar{1}\bar{1}]$, and the z-axis is along $[\bar{1}\bar{1}20]$ and [111]. It contains 16 periodic units for Mg and 11 periodic units for Nb in the x-direction, and 16 periodic units for Mg and 18 periodic units for Nb in the z-direction. The final dimensions of the bicrystal model are 8.885 nm and 5.137 nm in the x and z directions, corresponding to a super boundary unit cell at equilibrium. The bicrystal model is then relaxed for 100 ps at T = 10 K and then followed by quenching molecular dynamics until the forces acting on each atom is less than 5 pN. During relaxation, the two crystals are allowed to translate in the three orthogonal x-y-z directions, but restricted from rotating about the interface normal. The net forces, acting parallel and perpendicular to the interface, drive the translations.

2.3. Characterizing interface dislocations with AIFB

Characterizing interface dislocations is accomplished using atomically informed Frank-Bilby (AIFB) method [47–49]. AIFB was developed to determine interface misfit dislocations by combining the classical Frank-Bilby (F-B) theory and interface atomic structures obtained from atomistic simulations. Burgers vectors of possible misfit dislocations are defined in a trial reference lattice and will be modified after the real reference lattice is determined. Disregistry analysis is performed for the relaxed, equilibrium interface to identify misfit dislocations including lines and average spacing of interface dislocations, and areas containing coherent interfaces separated by interface dislocations.

The procedure of solving the F-B equation is described as follows. The lattices A and B at a given OR are related to a reference lattice (coherent/commensurate dichromatic pattern, CDP) by homogeneous distortion transformation matrices S_A and S_B. For an

Table 1
The fitted properties of the newly constructed EAM cross potentials for the Mg-Nb systems. ΔH is the heat of mixing. a_{CsCl} is lattice constant, and B_{CsCl} is bulk modulus of MgNb in CsCl structure. The fitted parameters of the newly constructed EAM cross potentials for the Mg-Nb systems are also provided.

	ΔH (Nb in Mg) (eV)	ΔH (Mg in Nb) (eV)	a_{CsCl} (Å)	B_{CsCl} (GPa)
VASP	1.24	1.16	3.35	94.6
Mg-Nb potential	1.23	1.19	3.47	94.6
Fitted parameters				
D_M	α_M	R_M	r_{cut}	
3.73752778	−0.569194529	1.73517317	3.97784756	
g_{Mg}	g_{Nb}	s_{Nb}		
13.9192097	0.0480312867	0.00600985599		

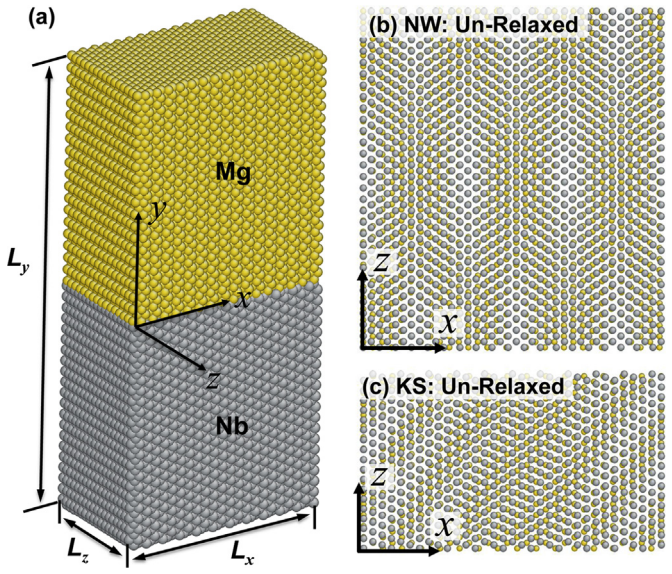

Fig. 2. (a) Schematic of simulation cells, (b) un-relaxed KS interface and (c) un-relaxed NW interface. The grey atoms and yellow atoms are Nb and Mg, respectively. The x-axis is along $[\bar{1}100]_{Mg}$ and $[110]_{Nb}$, and the z-axis is along $[\bar{1}\bar{1}20]_{Mg}$ and $[001]_{Nb}$ at the NW interface; the x-axis is along $[\bar{1}100]_{Mg}$ and $[2\bar{1}\bar{1}]_{Nb}$, and the z-axis is along $[\bar{1}\bar{1}20]_{Mg}$ and $[111]_{Nb}$ at the KS interface. (For interpretation of the references to colour in this figure legend, the reader is referred to the web version of this article.)

atomically flat interface, the transformation is 2 × 2 matrices. Let $\boldsymbol{p}$ be a probe vector in the interface, Burgers vector content $\boldsymbol{B}(\boldsymbol{p})$ at an equilibrium interface crossing $\boldsymbol{p}$ can be calculated as

$$\boldsymbol{B}(p) = \left(S_B^{-1} - S_A^{-1}\right)p \tag{5}$$

where S_A^{-1} and S_B^{-1} are the inverse matrices of S_A and S_B. Following Knowles' suggestion [58] that the discrete Burgers vectors of interface dislocations are the lattice vectors in the reference lattice, $\boldsymbol{B}(\boldsymbol{p})$ can be expressed in the reference lattice as

$$B(p) = \sum_{i=1}^{N}\left(\frac{n \times \overrightarrow{\xi_i}}{d_i}\cdot p\right)b_i \tag{6}$$

where N is the number of discrete interface dislocations, $\boldsymbol{b}_i$ is the Burgers vector of the ith interface dislocation, $\boldsymbol{n}$ is the interface normal, and ξ_i and d_i are the line sense and spacing of the ith interface dislocation, respectively. To solve the above equations, it is essential to know the Burgers vector content at the interface, the number of dislocations, the dislocation lines, the spacing of dislocation lines, coherent interfaces, and Burgers vectors of possible interface dislocations. The first one is easily computed from Equation (5), the second to fifth ones can be obtained from atomistic simulations, and Burgers vectors of possible interface dislocations can be the lattice vectors in the reference lattice.

A trial reference lattice is constructed by geometrically averaging the two lattices. Useful reference structures are often interfaces in which one or two directions in the interface are nearly commensurate in both crystal lattices, enabling coincidence site lattices (CSLs) to be generated. With a trial reference lattice, disregistry analysis is performed to characterize interface dislocations. In the disregistry analysis, pairs of atoms that straddle the desired interface plane are first identified in the un-relaxed interface. Three sets of vectors with respect to three structures (un-relaxed structure, relaxed structure, and CDP) are calculated with the identified i-j pairs: r_{ij}^{CDP} is the vector from atom i to j in the trial reference lattice, r_{ij}^{UnR} is the vector from atom i to j in the un-relaxed interface (referred to natural dichromatic pattern (NDP)), and r_{ij}^{Rlx} is the vector from atom i to j in the relaxed, equilibrium interface. The vector $r_{ij}^{U-C} = r_{ij}^{UnR} - r_{ij}^{CDP}$ describes the relative displacements corresponding to the distortion from a NDP to a CDP. Along a given probe vector, it will define the uniformly continuous distribution of interface Burgers vectors. The vector $r_{ij}^{R-C} = r_{ij}^{Rlx} - r_{ij}^{CDP}$ describes the relative displacements corresponding to the distortion from the relaxed interface to a CDP. Along a given probe vector, it will define the non-uniformly continuous distribution of interface Burgers vectors along the probe vector. The vector $r_{ij}^{R-U} = r_{ij}^{Rlx} - r_{ij}^{UnR}$ describes the relative displacements corresponding to the distortion from the relaxed interface to a NDP. It defines the non-uniform relaxation displacement due to the formation of discrete interface dislocations. Within a periodic length of the BUC, the net vector r_{ij}^{R-U} along the probe vector is zero. The displacements on opposite sides along the dislocation line have opposite sign. Thus, the vector fields of r_{ij}^{R-C} and r_{ij}^{R-U} along the probe vector will provide the necessary information for determining the position of discrete interface dislocations in a real bicrystal interface. Once interface dislocations including line sense, Burgers vector and spacing are determined with respect to a trial reference lattice from atomistic simulations, the real reference lattice can be obtained by solving the F-B equations.

3. Characterization of interface dislocations

3.1. NDP, CDP and RCDP

NDP is referred to as natural dichromatic pattern of two crystals in the interface plane. Fig. 3a shows the NDP according to the NW OR, where $\vec{e}_x^{Mg} = a_{Mg}[\bar{1}100]$ is parallel to $\vec{e}_x^{Nb} = a_{Nb}[110]$, and $\vec{e}_z^{Mg} = \frac{a_{Mg}}{3}[\bar{1}\bar{1}20]$ is parallel to $\vec{e}_z^{Nb} = a_{Nb}[001]$. Fig. 3b shows the NDP according to the KS OR, where $\vec{e}_x^{Mg} = a_{Mg}[\bar{1}100]$ is parallel to

$\vec{e}_x^{Nb} = a_{Nb}[2\bar{1}\bar{1}]$, and $\vec{e}_z^{Mg} = \frac{a_{Mg}}{3}[\bar{1}\bar{1}20]$ is parallel to $\vec{e}_z^{Nb} = \frac{a_{Nb}}{2}[111]$. CDP is referred to as the commensurate/coherent dichromatic pattern of the two crystals in the interface, where one or two directions are nearly commensurate in the two crystal lattices in order to generating CSLs. When two NDPs are similar and can form a CDP without a twist, two unknown parameters χ_x and χ_z (the geometric partition of the mismatch strain along two commensurate directions) are introduced to construct the CDP, such as in the NW case. If a twist is involved, a rotated CDP (RCDP) is required and a third unknown parameter χ_θ is introduced to describe the twist angle between the two NDPs.

The two crystals with the NW OR hold the parallelism of two commensurate directions and are only subjected to uniform compression or expansion to form the coherent structure. A CDP of Mg/Nb interfaces can be defined with respect to the NW OR as follows. The six lattice sites in the CDP lattice can be geometrically calculated with the two parameters χ_x and χ_z which are introduced previously to describe partition of the mismatch strains.

$$
\begin{aligned}
C(1) &= \left(\frac{\sqrt{2}}{2}a_{Nb} + \chi_x\left(\frac{\sqrt{3}}{2}a_{Mg} - \frac{\sqrt{2}}{2}a_{Nb}\right),\ \frac{1}{2}a_{Nb} - \chi_z\left(\frac{1}{2}a_{Nb} - \frac{1}{2}a_{Mg}\right)\right)\\
C(2) &= \left(0,\ a_{Nb} - \chi_z(a_{Nb} - a_{Mg})\right)\\
C(3) &= \left(-\frac{\sqrt{2}}{2}a_{Nb} - \chi_x\left(\frac{\sqrt{3}}{2}a_{Mg} - \frac{\sqrt{2}}{2}a_{Nb}\right),\ \frac{1}{2}a_{Nb} - \chi_z\left(\frac{1}{2}a_{Nb} - \frac{1}{2}a_{Mg}\right)\right)\\
C(4) &= \left(-\frac{\sqrt{2}}{2}a_{Nb} - \chi_x\left(\frac{\sqrt{3}}{2}a_{Mg} - \frac{\sqrt{2}}{2}a_{Nb}\right),\ -\frac{1}{2}a_{Nb} + \chi_z\left(\frac{1}{2}a_{Nb} - \frac{1}{2}a_{Mg}\right)\right)\\
C(5) &= \left(0,\ -a_{Nb} + \chi_z(a_{Nb} - a_{Mg})\right)\\
C(6) &= \left(\frac{\sqrt{2}}{2}a_{Nb} + \chi_x\left(\frac{\sqrt{3}}{2}a_{Mg} - \frac{\sqrt{2}}{2}a_{Nb}\right),\ -\frac{1}{2}a_{Nb} + \chi_z\left(\frac{1}{2}a_{Nb} - \frac{1}{2}a_{Mg}\right)\right)
\end{aligned}
\tag{7}
$$

The distortion matrices mapping the lattice vectors from the real lattices to the reference CDP lattice are

$$
S_{Mg} = \begin{bmatrix} \dfrac{\frac{\sqrt{2}}{2}a_{Nb} + \chi_x\left(\frac{\sqrt{3}}{2}a_{Mg} - \frac{\sqrt{2}}{2}a_{Nb}\right)}{\frac{\sqrt{3}}{2}a_{Mg}} & 0 \\ 0 & \dfrac{a_{Nb} - \chi_z(a_{Nb} - a_{Mg})}{a_{Mg}} \end{bmatrix}
$$

$$
S_{Nb} = \begin{bmatrix} \dfrac{\frac{\sqrt{2}}{2}a_{Nb} + \chi_x\left(\frac{\sqrt{3}}{2}a_{Mg} - \frac{\sqrt{2}}{2}a_{Nb}\right)}{\frac{\sqrt{2}}{2}a_{Nb}} & 0 \\ 0 & \dfrac{a_{Nb} - \chi_z(a_{Nb} - a_{Mg})}{a_{Nb}} \end{bmatrix}
\tag{8}
$$

The possible Burgers vectors of full dislocations defined in the CDP lattice are

$$
\begin{aligned}
b^{I} &= \left[\frac{\sqrt{2}}{2}a_{Nb} + \chi_x\left(\frac{\sqrt{3}}{2}a_{Mg} - \frac{\sqrt{2}}{2}a_{Nb}\right), \frac{1}{2}a_{Nb} - \chi_z\left(\frac{1}{2}a_{Nb} - \frac{1}{2}a_{Mg}\right)\right]\\
b^{II} &= \left[-\frac{\sqrt{2}}{2}a_{Nb} - \chi_x\left(\frac{\sqrt{3}}{2}a_{Mg} - \frac{\sqrt{2}}{2}a_{Nb}\right), \frac{1}{2}a_{Nb} - \chi_z\left(\frac{1}{2}a_{Nb} - \frac{1}{2}a_{Mg}\right)\right]\\
b^{III} &= \left[0, -a_{Nb} + \chi_z(a_{Nb} - a_{Mg})\right]
\end{aligned}
\tag{9}
$$

Comparing crystallography of the KS OR with the NW OR, the KS interface can be created through twisting the KS a rotation angle of 5.3° about the interface normal. Thus, the reference lattice for the KS interface can be obtained by rotating the CDP about $\theta_{CDP} = \theta_{Nb} + \chi_\theta(\theta_{Mg} - \theta_{Nb})$, referred to as the RCDP. The parameter χ_θ represents partition of the twist angle into the two crystals. The six lattice sites in the RCDP lattice are

$$
C_R(i) = \begin{bmatrix} \cos(\theta_{Nb} + \chi_\theta(\theta_{Mg} - \theta_{Nb})) & -\sin(\theta_{Nb} + \chi_\theta(\theta_{Mg} - \theta_{Nb})) \\ \sin(\theta_{Nb} + \chi_\theta(\theta_{Mg} - \theta_{Nb})) & \cos(\theta_{Nb} + \chi_\theta(\theta_{Mg} - \theta_{Nb})) \end{bmatrix} C(i)
\tag{10}
$$

Correspondingly, the Burgers vectors of possible full dislocations defined in the RCDP lattice are

$$
b_R(i) = \begin{bmatrix} \cos(\theta_{Nb} + \chi_\theta(\theta_{Mg} - \theta_{Nb})) & -\sin(\theta_{Nb} + \chi_\theta(\theta_{Mg} - \theta_{Nb})) \\ \sin(\theta_{Nb} + \chi_\theta(\theta_{Mg} - \theta_{Nb})) & \cos(\theta_{Nb} + \chi_\theta(\theta_{Mg} - \theta_{Nb})) \end{bmatrix} b(i)
\tag{11}
$$

Such a two-dimensional hexagonal close-packed lattice (CDP) can be stacked into three coherent structures with respect to in-pane translations: normal fcc structures (FCC in Fig. 3c), low-energy stacking faulted structures (SF in Fig. 3d), and high-energy stacking faulted structures (HESF in Fig. 3e). It is worth mentioning that a relaxed interface could comprise multiple coherent structures, as have been explored in fcc/fcc interfaces [59–61] and NbC-Nb interfaces [62]. Taking fcc/fcc (111) interfaces as an example, there are three coherent interfaces, FCC, SF and HESF. Due to the metastable nature of HESF structure, a relaxed fcc/fcc interface is composed of two coherent interface structures: FCC and SF. Corresponding to this crystallographic feature, Shockley partial dislocations instead of full dislocations are identified on fcc/fcc (111) interfaces and separate the interface into FCC and SF

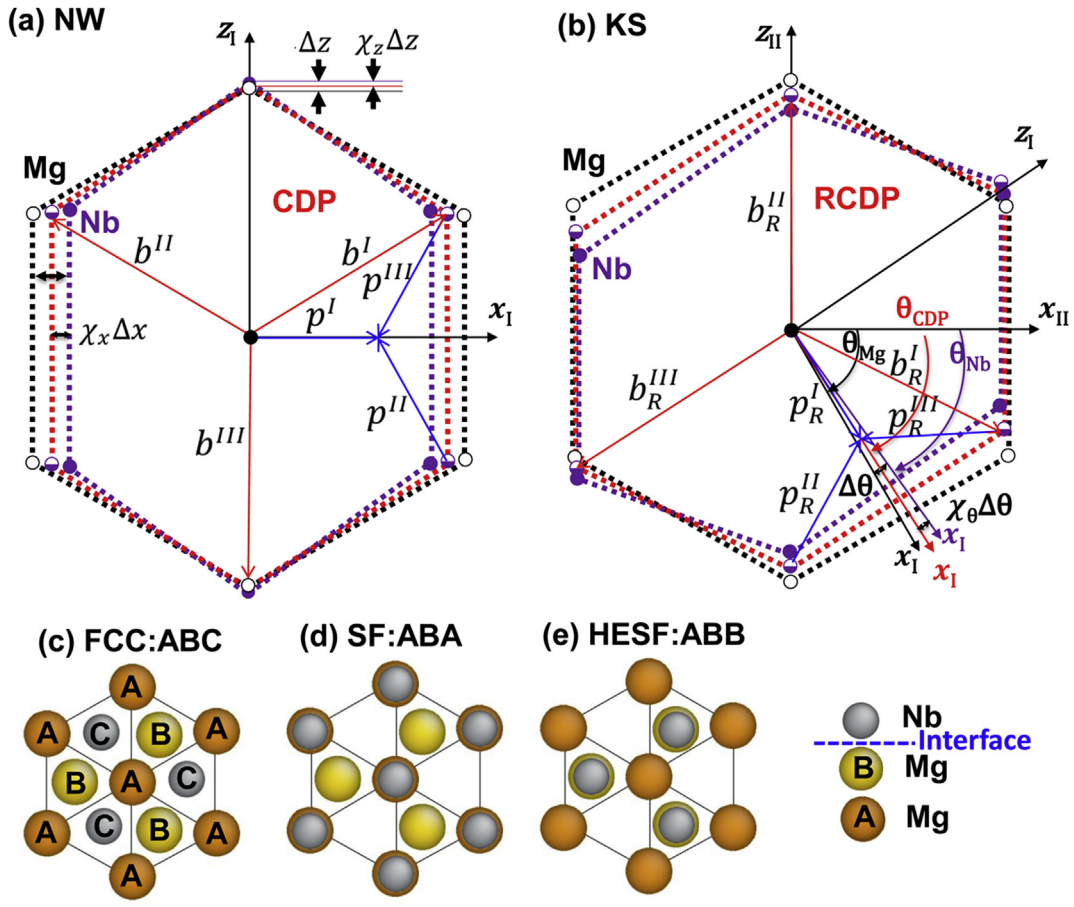

Fig. 3. (a) Commensurate/coherent dichromatic pattern and natural dichromatic pattern (NDP) of Mg/Nb interface with the Nishiyama-Wassermann (NW) orientation relationship, and (b) the rotation CDP (RCDP) and NDP of Mg/Nb interface with the Kurdjumov-Sachs (KS) orientation relationship. The black empty and purple solid circles represent atomic sites of Mg and Nb, respectively, forming the NDPs. The mixed circles represent the CDP/RCDP lattices. Three variables, χ_x, χ_z, and χ_θ are introduced to characterize partition of lattice mismatch in the NDPs associated with formation of the CDP and RCDP lattices. Possible full and partial dislocations in each orientation relationship are marked. (c)–(e) illustrate three coherent structures: (c) fcc interface (FCC), (d) low-energy stacking faulted (SF) interface and (e) high-energy stacking faulted interface (HESF). A, B, and C refer to the relative positions of hexagonal close packed planes in terms of the stacking sequence of (111) planes in a fcc structure. (For interpretation of the references to colour in this figure legend, the reader is referred to the web version of this article.)

coherent regions. Here, we thus define three partial dislocations in the CDP lattice (NW) and RCDP lattice (KS). The Burgers vectors of three possible partial dislocations defined in CDP lattice on the NW interface are

$$p^I = \left[\frac{\sqrt{2}}{3}a_{Nb} + \chi_x\left(\frac{\sqrt{3}}{3}a_{Mg} - \frac{\sqrt{2}}{3}a_{Nb}\right), 0\right]$$

$$p^{II} = \left[-\frac{\sqrt{2}}{6}a_{Nb} - \chi_x\left(\frac{\sqrt{3}}{6}a_{Mg} - \frac{\sqrt{2}}{6}a_{Nb}\right), \frac{1}{2}a_{Nb} - \chi_z\left(\frac{1}{2}a_{Nb} - \frac{1}{2}a_{Mg}\right)\right]$$

$$p^{III} = \left[-\frac{\sqrt{2}}{6}a_{Nb} - \chi_x\left(\frac{\sqrt{3}}{6}a_{Mg} - \frac{\sqrt{2}}{6}a_{Nb}\right), -\frac{1}{2}a_{Nb} + \chi_z\left(\frac{1}{2}a_{Nb} - \frac{1}{2}a_{Mg}\right)\right] \quad (12)$$

and the Burgers vectors of three possible partial dislocations defined in the RCDP lattice on the KS interface are

$$p_R(i) = \begin{bmatrix} \cos(\theta_{Nb} + \chi_\theta(\theta_{Mg} - \theta_{Nb})) & -\sin(\theta_{Nb} + \chi_\theta(\theta_{Mg} - \theta_{Nb})) \\ \sin(\theta_{Nb} + \chi_\theta(\theta_{Mg} - \theta_{Nb})) & \cos(\theta_{Nb} + \chi_\theta(\theta_{Mg} - \theta_{Nb})) \end{bmatrix} p(i) \quad (13)$$

3.2. Coherent structures of Mg/Nb interfaces

Using molecular statics (MS) method, we compute the generalized stacking fault energy profile (γ-surface) of Mg/Nb coherent interfaces. The simulation cell of the coherent structure with NW orientation relationship contains 8 periodicity-lengths along $[\bar{1}100]$ for Mg and 8 periodicity-lengths along [110] for Nb in the x direction, 12 periodicity-lengths along $[\bar{1}\bar{1}20]$ for Mg and 12 periodicity-lengths along [001] for Nb in the z direction. The heights of Mg and Nb crystals in the *y*-direction are chosen to be ~6.5 nm each. The thickness of the fixed region in the *y*-direction is 1 nm (twice the cut-off distance of the interatomic potential) for the two crystals. The periodic boundary conditions are applied in the *x* and *z* directions. The two dimensions in the *x* and *z* directions are not arbitrarily chosen because of the mismatch nature of the Mg and Nb crystals, but determined according to equilibrium conditions [29] that normal stresses σ_{yy} in the two crystals are zero; the summation of stress σ_{xx} in the two crystals and the summation of stress σ_{zz} in the two crystals are zero. Periodicity requires equal dimensions in the *x* and *z* directions for the two crystals. The final dimension, solved from the six conditions, in the *x* direction is 4.0 nm, and in the *z* direction, 3.9 nm. To obtain the energy profile, the Mg crystal is shifted relative to the Nb crystal with incremental

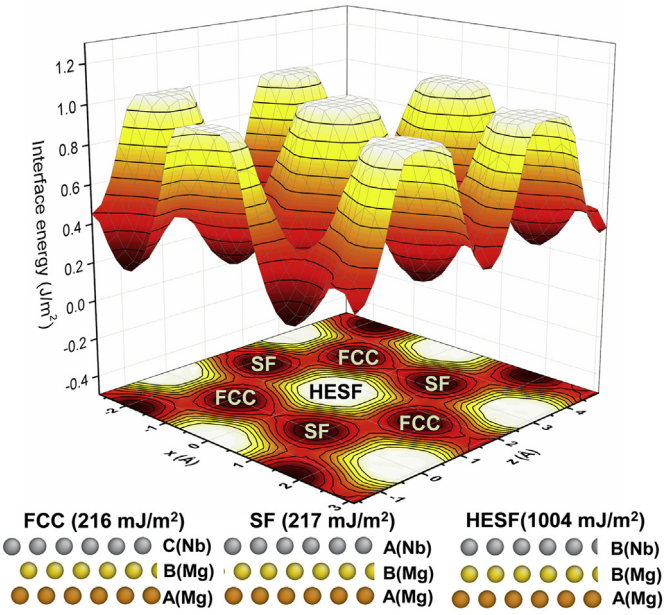

Fig. 4. The generalized stacking fault energy profile (γ-surface) of the coherent Mg/Nb interface, showing two low-energy coherent structures (FCC and SF interfaces) and one high-energy coherent structure (HESF).

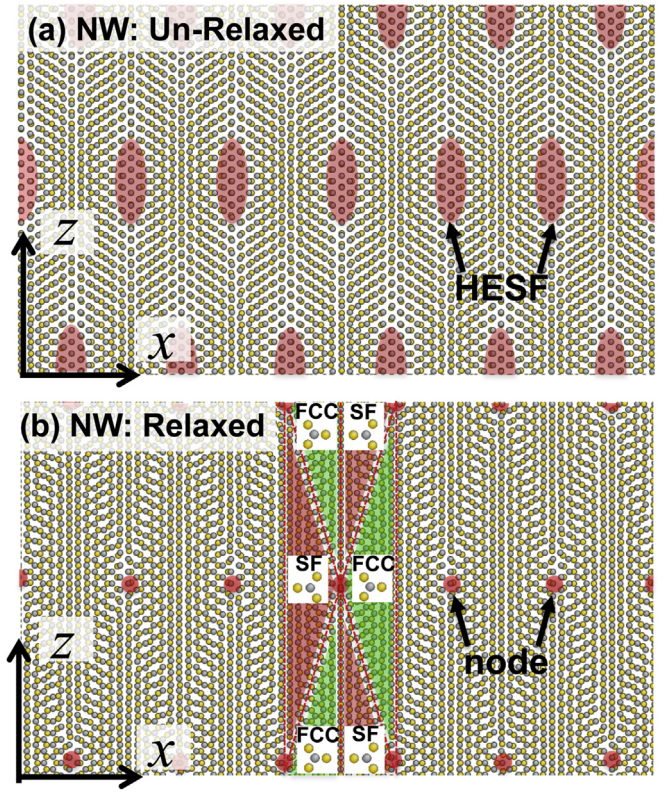

Fig. 5. Atomic structures of before (a) and after (b) relaxation of the NW interface. The grey atoms and yellow atoms are Nb and Mg, respectively. The x-axis is along $[\bar{1}100]_{Mg}$ and $[110]_{Nb}$, and the z-axis is along $[\bar{1}\bar{1}20]_{Mg}$ and $[001]_{Nb}$ at NW interface. HESF regions (a) that are marked in the un-relaxed structure relax into nodes (b) in the relaxed structure. Two types of coherent interface structures, FCC and SF, are marked in the green and red shadows in (b). (For interpretation of the references to colour in this figure legend, the reader is referred to the web version of this article.)

displacements by 0.2 Å/step along x and z directions respectively. During the structure relaxation, atoms are only allowed to move along the y direction. The interface energy is calculated by subtracting the elastic energy and cohesive energy in the strained Nb and Mg crystals from the total energy [19]. The γ-surface (Fig. 4) shows two stable coherent structures (FCC and SF) with low interface energy (216 mJ/m^2 for FCC structure and 217 mJ/m^2 for SF structure) and a metastable coherent structure (HESF) with a high interface energy (1004 mJ/m^2), which indicates that Mg/Nb interfaces could comprise two coherent structures (FCC and SF), similar to that presenting in fcc/fcc (111) interface with low interface stacking fault energy [59–61]. Therefore, misfit dislocations in Mg/Nb interfaces are speculated to be partial dislocations instead of full dislocations.

3.3. Dislocation structures of the NW interface

For the NW interface, Fig. 5 shows atomic structures of the un-relaxed and relaxed Mg/Nb interfaces. Corresponding to crystallographic analysis of the un-relaxed Mg/Nb interface, HESF regions are identified in Fig. 5a, as highlighted in the orange ellipses. After relaxation, these HESF regions shrink into nodes in Fig. 5b. Most importantly, we identify six interface regions around a node. These coherent interface regions take either FCC structure or SF structure, as indicated in Fig. 5b. Thus, interface misfit dislocations must be partial dislocations.

The disregistry plot of the vector fields r_{ij}^{R-U} is shown in Fig. 6a. The disregistry vectors r_{ij}^{R-C} and r_{ij}^{U-C} are plotted in Fig. 6b as the probe vector is along the x-direction. Fig. 6c shows the disregistry r_{ij}^{R-U} corresponding to the difference between the disregistry vectors r_{ij}^{R-C} and r_{ij}^{U-C} in Fig. 6b. The non-uniform displacement fields in Fig. 6b are associated with the formation of discrete interface dislocations as indicated by the green solid lines in Fig. 6a and dislocation symbols in Fig. 6c. The magnitudes of these displacements cannot be used to define the Burgers vectors of these interface dislocations especially for the case when the interface contains a high-density of dislocations, because these displacements are a summation of all dislocations at a position. From the above analysis with multiple probe vectors, three sets of dislocation lines are correspondingly determined in the relaxed interface. One is along the z-axis with the averaging spacing of 1.47 nm and referred to as $\mathbf{b_1}$. The other two, $\mathbf{b_2}$ and $\mathbf{b_3}$, are inclined with the angles of 73° and 107° with respect to the x-axis, and their averaging spacing is 2.81 nm. The line senses and Burgers vectors of these dislocations are further identified according to the local shear displacement in the coherent regions. Fig. 7a shows a disregistry plot with respect to the CDP around a node. Comparing the shear in each region with the possible partial dislocations defined in Fig. 3a, the six coherent interface regions can be created by nucleating and propagating six partial dislocation loops, p^I, $-p^{II}$, p^{III}, $-p^I$, p^{II}, and $-p^{III}$ with respect to the reference lattice, as schematically shown in Fig. 7b. Thus, formation of interface dislocations, $\mathbf{b_1}$, $\mathbf{b_2}$ and $\mathbf{b_3}$, is a result of the reaction between these partial dislocation loops. The line senses and Burgers vectors of $\mathbf{b_1}$, $\mathbf{b_2}$ and $\mathbf{b_3}$ are well defined in Fig. 7b.

We so far have determined line senses, types of Burgers vectors, and average spacing of interface dislocations in the relaxed NW interface. With these as input, we obtain the real CDP and Burgers vectors of interface dislocations by solving the F-B equation. The two unknown parameters are determined to be $\chi_x = 0.5$ and $\chi_z = 1$ with respect to the simulation system. Table 2 summarize the line senses, Burgers vectors, and spacing of misfit dislocations.

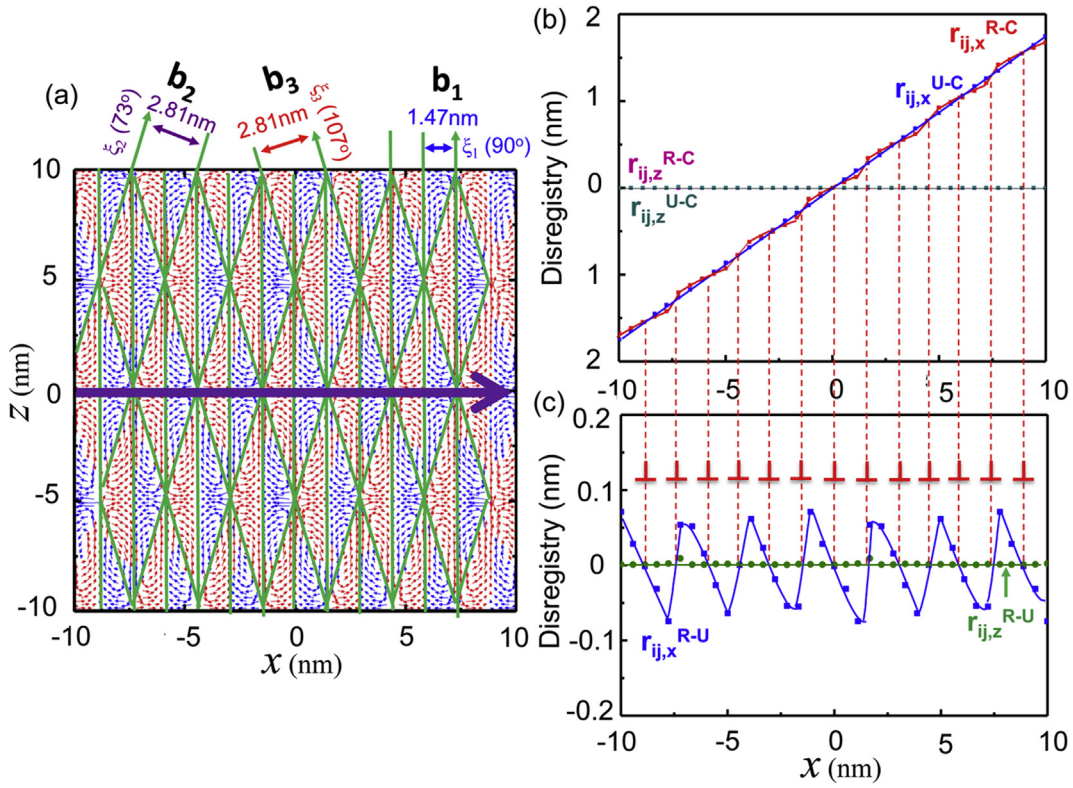

Fig. 6. Disregistry plots of the Mg/Nb interface showing three sets of partial dislocations and two types of coherent interfaces. (a) The disregistry plot of the vector field r_{ij}^{R-U} at NW interface. The arrows show shear displacements in two coherent interface regions and are colored according to the shear direction. To identify interface dislocations, the disregistry vectors (b) r_{ij}^{R-C} and r_{ij}^{U-C} and (c) r_{ij}^{R-U} along the probe vector (z = 0 along the x-direction) are analyzed. $r_{ij,x \text{ and }} r_{ij,z}$ represent the x- and z-component of disregistry vectors. The positions of interface dislocations are marked as a dislocation symbol in (c). Multiple probe vectors along different directions were used to determine dislocation lines in (a). (For interpretation of the references to colour in this figure legend, the reader is referred to the web version of this article.)

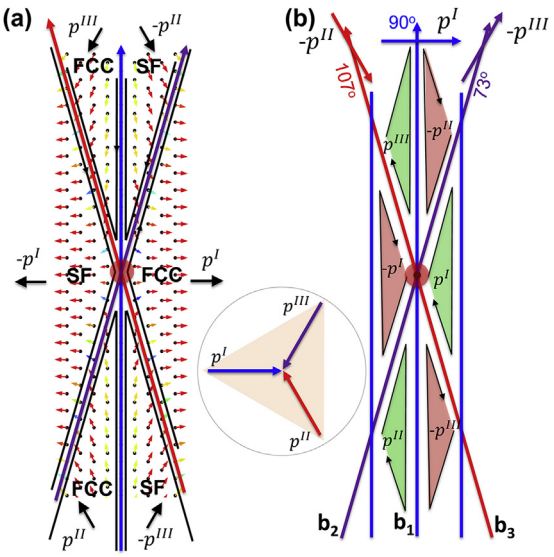

Fig. 7. Dislocation structures around a node. (a) Disregistry plots in the six coherent interface regions, and (b) schematic of formation mechanisms of coherent interfaces and interface dislocations.

3.4. Dislocation structures of the KS interface

For the KS interface, Fig. 8 shows atomic structures of the un-relaxed and relaxed Mg/Nb interfaces. According to a crystallographic analysis of the un-relaxed Mg/Nb interface, HESF regions are clearly identified in Fig. 8a', as highlighted in the orange ellipses. After relaxation, these HESF regions shrink into nodes in Fig. 8a due to the high interface energy. Similar to the analysis in the NW case, we identify six interface regions around a node. These coherent interface regions take either FCC structure or SF structure, as indicated in Fig. 8a and schematically shown in Fig. 8b. Thus, there could be three sets of partial dislocations, $\mathbf{b_1}$, $\mathbf{b_2}$ and $\mathbf{b_3}$, as denoted by the blue, red and purple solid lines.

We further perform disregistry analysis for the relaxed interface around a node with respect to RCDP lattice, as shown in Fig. 9. Fig. 9a shows a disregistry plot around a node. Comparing the shear in each coherent region with the possible partial dislocations defined in Fig. 3b, the six coherent interface regions can be created by nucleating and propagating of six partial dislocation loops, p_R^I, $-p_R^{III}$, p_R^{II}, $-p_R^I$, p_R^{III}, and $-p_R^{II}$ with respect to the reference lattice, as schematically shown in Fig. 9b. It is noticed that two regions associated with partial dislocation loops p_R^{III} and $-p_R^{III}$ are difficult to distinguish around the node. We identified them according to the region away from the node. Thus, we can define interface dislocations, $\mathbf{b_1}$, $\mathbf{b_2}$ and $\mathbf{b_3}$, by performing reactions between these partial dislocation loops. Correspondingly, interface dislocation $\mathbf{b_1}$ has the dislocation line along the z-axis, Burgers vector $-p_R^{III}$, and averaging spacing of 8.89 nm; interface dislocation $\mathbf{b_2}$ has the dislocation line 57.6° inclined with respect to the x-axis, Burgers vector p_R^I, and averaging spacing of 1.35 nm; interface dislocation $\mathbf{b_3}$ has the dislocation line 56.1° inclined with respect to the x-axis, Burgers vector $-p_R^{II}$, and averaging spacing of 1.48 nm. With these parameters as input, we obtain the real RCDP lattice and Burgers vectors of interface dislocations by solving the F-B equation. The third

Table 2
A summary of line sense, spacing and Burgers vectors of interface dislocations of the NW interface and KS interfaces. KS* represents the real distribution of interface dislocations.

		Line sense (ξ)	Spacing (d)	Burgers vector (b)
NW	Set 1	90°	1.47 nm	p^{I}
	Set 2	73°	2.81 nm	$-p^{III}$
	Set 3	107°	2.81 nm	$-p^{II}$
KS	Set 1	90°	8.89 nm	$-p_R^{III}$
	Set 2	57.6°	1.35 nm	p_R^{I}
	Set 3	56.1°	1.48 nm	$-p_R^{II}$
KS*	Set 1	90°	8.89 nm	$-p_R^{III}$
	Set 2 (segments)	90°	8.89 nm	p_R^{I}
	Set 3 (segments)	90°	8.89 nm	$-p_R^{II}$
	Set 4	56.8°	1.40 nm	$-b_R^{II}$

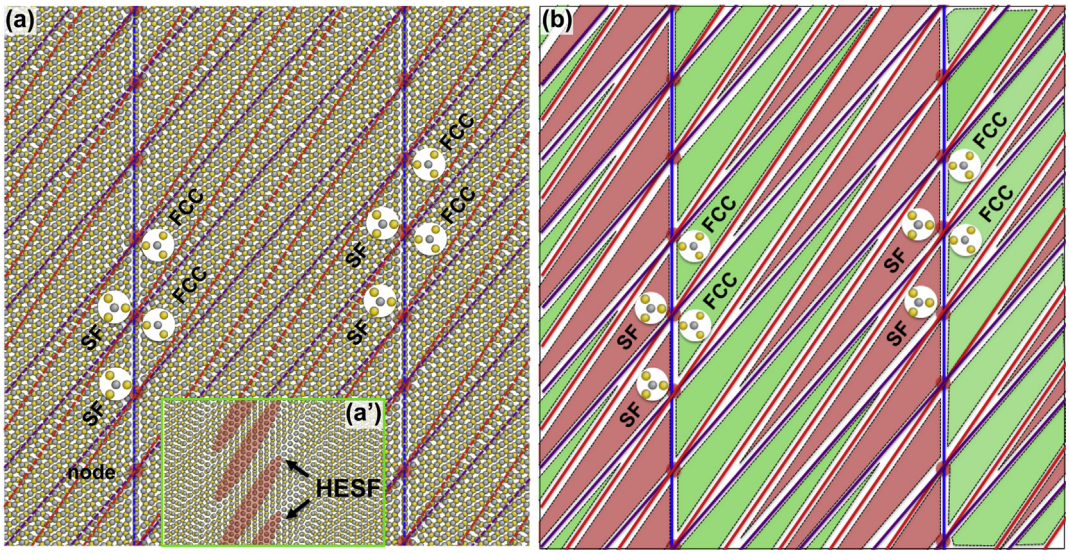

Fig. 8. Atomic structures of before (a′) and after (a) relaxation of the KS interface. The grey atoms and yellow atoms are Nb and Mg, respectively. The x-axis is along $[\bar{1}100]_{Mg}$ and $[2\bar{1}\bar{1}]_{Nb}$, and the z-axis is along $[\bar{1}\bar{1}20]_{Mg}$ and $[111]_{Nb}$ at KS interface. HESF regions in the un-relaxed structure and dislocation nodes in the relaxed structure are marked in orange ellipses and dots, respectively. HESF regions (a′) that are marked in the un-relaxed structure relax into nodes (b) in the relaxed structure. Two types of coherent interface structures, FCC and SF, are marked in the green and red shadows in (b). (For interpretation of the references to colour in this figure legend, the reader is referred to the web version of this article.)

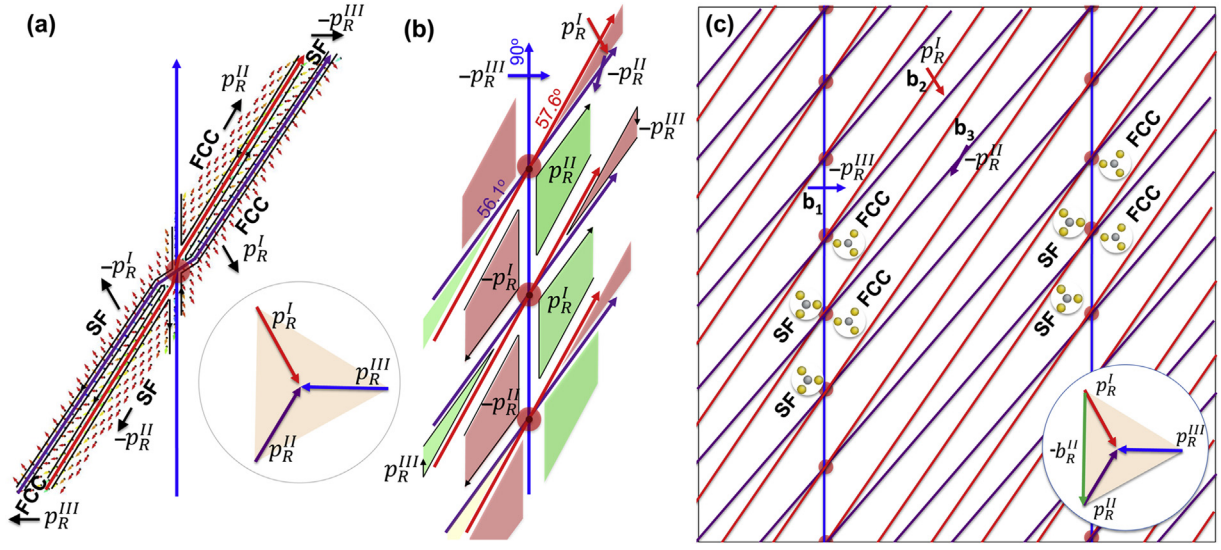

Fig. 9. Dislocation structures around a node, showing (a) Disregistry plots in the six coherent interface regions, (b) schematic of formation mechanisms of coherent interfaces and interface dislocations, and (c) schematic of interface dislocations.

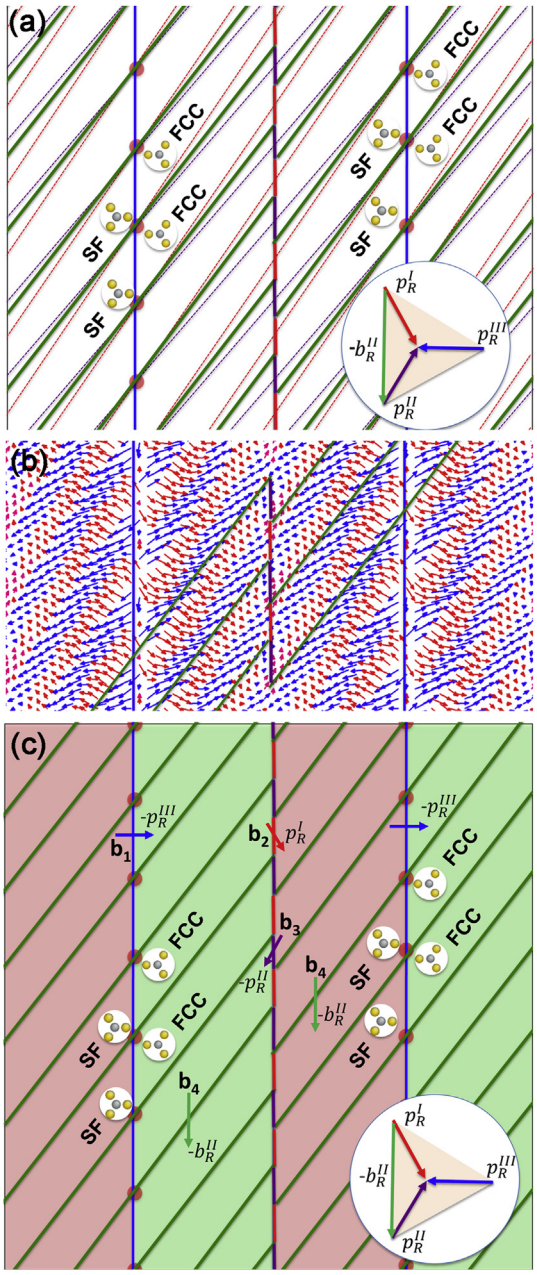

Fig. 10. Interface dislocations of the KS interface, showing (a) reaction of partial dislocation dislocations, (b) disregistry plot, and (c) schematic of interface dislocations and interface coherent structures.

unknown parameter χ_θ is determined to be 0.7 with respect to the simulation system. Table 2 summarizes the lines, Burgers vectors, and spacing of interface dislocations.

It is noted that the two regions associated with partial dislocation loops p_R^{III} and $-p_R^{III}$ in Fig. 9a are quite narrow around a node. This is ascribed to the small spacing (0.7 nm) between two misfit dislocations $\mathbf{b_2}$ and $\mathbf{b_3}$. In reality, the two partial dislocations can be treated as a full dislocation $\mathbf{b_4}$ ($=-b_R^{II}$) because the spacing is less than the core width of partial dislocations, as schematically shown in Fig. 10a. This is consistent with the disregistry feature (with respect to un-relaxed structure) of the relaxed KS interface (Fig. 10b). As a result, the KS interface is composed of four sets of interface dislocations and two types of coherent interfaces, referred to as KS* (Fig. 10c and Table 2). The Burgers vector of the resultant dislocation is one of possible Burgers vectors (b_R^{II}) defined in the reference state (Fig. 3), and its line bisects the two partial dislocations.

4. Conclusions

From the perspective of stacking sequences of hcp/bcc interfaces, the feature of interface dislocation networks of hcp (0001)/bcc (110) interface was thought to be similar to that of fcc (111)/bcc (110) interface, as hcp (0001) close-packed plane is similar to fcc (111) plane. However, we found significant differences in the interface structures between these two systems: two low-energy coherent interfaces and partial dislocations at the hcp/bcc interface (Mg/Nb), in contrast to one low-energy coherent interface and full dislocations at the fcc/bcc interface (Cu/Nb). Therefore, the analysis of coherent structures should be prerequisite to identify the interface dislocations. Correspondingly, a generalized characterization procedure was proposed.

The generalized stacking fault energy profile (γ-surface) of the coherent Mg/Nb interface was used to screen low-energy coherent structures. The importance of this calculation lies in that the character of interface misfit dislocations could be inferred by the feature and number of coherent interfaces. For instance, in Mg/Nb, two types of low-energy coherent structures (FCC and SF stacking) require partial dislocations to separate different coherent regions, while in Cu/Nb, the existence of only one type of low-energy coherent structure (FCC) implies that only full dislocations are required at the interface to separate the coherent structures [47,48].

The disregistry analyses with respect to both un-relaxed structure and CDP/RCDP were performed. For the disregistry in reference to the un-relaxed structure, the Burgers vector content within a periodic length of the BUC is zero, thus disregistry analysis could be employed to illustrate the overall feature of dislocation network, such as the line sense, spacing and location of dislocations. However, when the dislocation density is high, dislocation cores may overlap, making the identification of individual dislocations difficult. Therefore, the identification of coherent regions (disregistry with the reference of CDP/RCDP) around one node is necessary to assist dislocation characterization. Assuming that these coherent regions form by nucleation and propagation of dislocation loops, the location and Burgers vectors of interface dislocations can be obtained by the reaction of these dislocation loops. For instance, in NW Mg/Nb, the six coherent interface regions can be identified along with six partial dislocation loops and the formation of interface dislocations as a result of the reaction between these partial dislocation loops. Since the dislocation cores in NW Mg/Nb are not significantly overlapped, the features of dislocations from both disregistry analyses are the same. In contrast, in KS Mg/Nb, the cores of two sets of partial dislocations overlap significantly and therefore the identification of coherent regions (disregistry with respect to RCDP) near a node is necessary to assist in the dislocation analysis. Finally, since the line senses, characters, and locations of dislocations are obtained, real CDP and RCDP with precise Burgers vectors of interface dislocations can be determined by F-B theory.

Finally, we note that the disregistry in coherent regions near a node can indicate the shear in overlapped dislocation core regions. In real crystals, overlapped dislocation cores react and form new dislocations. For instance, in KS Mg/Nb (Fig. 10), two nearby partial dislocations will react into full dislocations. Without the assistance of the disregistry analysis in coherent regions near a node, it is difficult to characterize interface dislocations by regular disregistry analysis due to severe core overlap. It is worth mentioning that this generalized procedure is applicable not only to the hcp/bcc interface, but also other systems with complicated interface dislocation

configurations.

In summary, we characterized interface dislocations of Mg/Nb interfaces with NW and KS ORs and proposed a generalized procedure of characterizing interface structure. In Mg/Nb, interface dislocation networks of the two types of interfaces are significantly different although they originate from similar partial dislocations: the NW interface is composed of three sets of partial dislocations, while the KS interface is composed of four sets of interface dislocations - three sets of partial dislocations and one set of full dislocation that forms from the reaction of two close partial dislocations. Further work will be focused on understanding thermodynamic properties and mechanical response of Mg/Nb interfaces.

Acknowledgements

J. Wang acknowledges funding from the Nebraska Center for Energy Sciences and Research. This work was partly supported by the U.S. Department of Energy, Office of Science, Office of Basic Energy Sciences. S. Shao acknowledges the support of start-up grant provided by the Louisiana State University. This work was performed, in part, at the Center for Integrated Nanotechnologies, an Office of Science User Facility operated for the U.S. Department of Energy (DOE) Office of Science. Los Alamos National Laboratory, an affirmative action equal opportunity employer, is operated by Los Alamos National Security, LLC, for the National Nuclear Security Administration of the U.S. Department of Energy under contract DE-AC52-06NA25396.

References

[1] F. Froes, Advanced metals for aerospace and automotive use, Mater. Sci. Eng. A 184 (1994) 119.
[2] B. Mordike, T. Ebert, Magnesium: properties—applications—potential, Mater. Sci. Eng. A 302 (2001) 37.
[3] J.W. Christian, S. Mahajan, Deformation twinning, Prog. Mater. Sci. 39 (1995) 1.
[4] P. Partridge, The crystallography and deformation modes of hexagonal close-packed metals, Metall. Rev. 12 (1967) 169.
[5] Q. Yu, Z.-W. Shan, J. Li, et al., Strong crystal size effect on deformation twinning, Nature 463 (2010) 335.
[6] M. Barnett, Twinning and the ductility of magnesium alloys: Part II."Contraction" twins, Mater. Sci. Eng. A 464 (2007) 8.
[7] Y. Chino, K. Sassa, A. Kamiya, et al., Enhanced formability at elevated temperature of a cross-rolled magnesium alloy sheet, Mater. Sci. Eng. A 441 (2006) 349.
[8] S.-H. Kim, B.-S. You, C.D. Yim, et al., Texture and microstructure changes in asymmetrically hot rolled AZ31 magnesium alloy sheets, Mater. Lett. 59 (2005) 3876.
[9] M.R. Barnett, Z. Keshavarz, A.G. Beer, et al., Influence of grain size on the compressive deformation of wrought Mg–3Al–1Zn, Acta Mater. 52 (2004) 5093.
[10] J.A. del Valle, F. . Carreño, O.A. Ruano, Influence of texture and grain size on work hardening and ductility in magnesium-based alloys processed by ECAP and rolling, Acta Mater. 54 (2006) 4247.
[11] A. Jain, O. Duygulu, D.W. Brown, et al., Grain size effects on the tensile properties and deformation mechanisms of a magnesium alloy, AZ31B, sheet, Mater. Sci. Eng. A 486 (2008) 545.
[12] W. Jian, G. Cheng, W. Xu, et al., Ultrastrong Mg alloy via nano-spaced stacking faults, Mater. Res. Lett. 1 (2013) 61.
[13] L.L. Rokhlin, Magnesium Alloys Containing Rare Earth Metals: Structure and Properties, Crc Press, 2003.
[14] T.L. Chia, M. Easton, S.-M. Zhu, et al., The effect of alloy composition on the microstructure and tensile properties of binary Mg-rare earth alloys, Intermetallics 17 (2009) 481.
[15] S. Tekumalla, S. Seetharaman, A. Almajid, et al., Mechanical properties of magnesium-rare earth alloy systems: a review, Metals 5 (2014) 1.
[16] B. Ham, X. Zhang, High strength Mg/Nb nanolayer composites, Mater. Sci. Eng. A 528 (2011) 2028.
[17] Y. Lu, R. Kotoka, J. Ligda, et al., The microstructure and mechanical behavior of Mg/Ti multilayers as a function of individual layer thickness, Acta Mater. 63 (2014) 216.
[18] A. Misra, J. Hirth, R. Hoagland, Length-scale-dependent deformation mechanisms in incoherent metallic multilayered composites, Acta Mater. 53 (2005) 4817.
[19] A. Kumar, I.J. Beyerlein, J. Wang, First-principles study of the structure of Mg/Nb multilayers, Appl. Phys. Lett. 105 (2014) 071602.
[20] N. Mara, D. Bhattacharyya, P. Dickerson, et al., Deformability of ultrahigh strength 5 nm Cu/Nb nanolayered composites, Appl. Phys. Lett. 92 (2008) 1901.
[21] N. Mara, D. Bhattacharyya, R. Hoagland, et al., Tensile behavior of 40nm Cu/Nb nanoscale multilayers, Scr. Mater. 58 (2008) 874.
[22] N. Mara, D. Bhattacharyya, J. Hirth, et al., Mechanism for shear banding in nanolayered composites, Appl. Phys. Lett. 97 (2010) 021909.
[23] J. Wang, A. Misra, An overview of interface-dominated deformation mechanisms in metallic multilayers, Curr. Opin. Solid State Mater. Sci. 15 (2011) 20.
[24] N.A. . Mara, I.J. Beyerlein, Review: effect of bimetal interface structure on the mechanical behavior of Cu-Nb fcc-bcc nanolayered composites, J. Mater. Sci. 49 (2014) 6497.
[25] J. Wang, A. Misra, Strain hardening in nanolayered thin films, Curr. Opin. Solid State Mater. Sci. 18 (2014) 19.
[26] J. Wang, C. Zhou, I.J. Beyerlein, et al., Modeling interface-dominated mechanical behavior of nanolayered crystalline composites, JOM 66 (2014) 102.
[27] I. Beyerlein, M. Demkowicz, A. Misra, et al., Defect-interface interactions, Prog. Mater. Sci. 74 (2015) 125.
[28] N.A. Mara, N. Li, A. Misra, et al., Interface-driven plasticity in metal–ceramic nanolayered composites: direct validation of multiscale deformation modeling via in situ indentation in TEM, JOM 68 (2016) 143.
[29] J. Wang, R. Hoagland, J. Hirth, et al., Atomistic simulations of the shear strength and sliding mechanisms of copper–niobium interfaces, Acta Mater. 56 (2008) 3109.
[30] M. Demkowicz, L. Thilly, Structure, shear resistance and interaction with point defects of interfaces in Cu–Nb nanocomposites synthesized by severe plastic deformation, Acta Mater. 59 (2011) 7744.
[31] R. Zhang, J. Wang, I. Beyerlein, et al., Atomic-scale study of nucleation of dislocations from fcc–bcc interfaces, Acta Mater. 60 (2012) 2855.
[32] I.J. Beyerlein, J. Wang, R. Zhang, Mapping dislocation nucleation behavior from bimetal interfaces, Acta Mater. 61 (2013) 7488.
[33] N. Gupta, M. . Baskes, S. Srinivasan, The role of interface structure in spallation of a layered nanocomposite, JOM 63 (2011) 74.
[34] J. Wang, K. Kang, R. Zhang, et al., Structure and property of interfaces in ARB Cu/Nb laminated composites, JOM 64 (2012) 1208.
[35] R. Zhang, T. Germann, J. Wang, et al., Role of interface structure on the plastic response of Cu/Nb nanolaminates under shock compression: non-equilibrium molecular dynamics simulations, Scr. Mater. 68 (2013) 114.
[36] J. Wang, R. Hoagland, X. Liu, et al., The influence of interface shear strength on the glide dislocation–interface interactions, Acta Mater. 59 (2011) 3164.
[37] J. Wang, A. Misra, R. Hoagland, et al., Slip transmission across fcc/bcc interfaces with varying interface shear strengths, Acta Mater. 60 (2012) 1503.
[38] H. Chu, J. Wang, I. Beyerlein, et al., Dislocation models of interfacial shearing induced by an approaching lattice glide dislocation, Int. J. Plast. 41 (2013) 1.
[39] J. Wang, R.G. Hoagland, A. Misra, Room-temperature dislocation climb in metallic interfaces, Appl. Phys. Lett. 94 (2009) 131910.
[40] N. Li, J. Wang, J. Huang, et al., In situ TEM observations of room temperature dislocation climb at interfaces in nanolayered Al/Nb composites, Scr. Mater. 63 (2010) 363.
[41] I.J. Beyerlein, N.A. Mara, D. Bhattacharyya, et al., Texture evolution via combined slip and deformation twinning in rolled silver–copper cast eutectic nanocomposite, Int. J. Plast. 27 (2011) 121.
[42] J. Wang, I.J. Beyerlein, N.A. Mara, et al., Interface-facilitated deformation twinning in copper within submicron Ag–Cu multilayered composites, Scr. Mater. 64 (2011) 1083.
[43] W. Han, J. Carpenter, J. Wang, et al., Atomic-level study of twin nucleation from face-centered-cubic/body-centered-cubic interfaces in nanolamellar composites, Appl. Phys. Lett. 100 (2012) 011911.
[44] S. Zheng, I. Beyerlein, J. Wang, et al., Deformation twinning mechanisms from bimetal interfaces as revealed by in situ straining in the TEM, Acta Mater. 60 (2012) 5858.
[45] S. Zheng, I.J. Beyerlein, J.S. Carpenter, et al., High-strength and thermally stable bulk nanolayered composites due to twin-induced interfaces, Nat. Commun. 4 (2013) 1696.
[46] N. Mara, I. Beyerlein, J. Carpenter, et al., Interfacially driven deformation twinning in bulk Ag-Cu composites, JOM 64 (2012) 1218.
[47] J. Wang, R. Zhang, C. Zhou, et al., Characterizing interface dislocations by atomically informed Frank-Bilby theory, J. Mater. Res. 28 (2013) 1646.
[48] J. Wang, R. Zhang, C. Zhou, et al., Interface dislocation patterns and dislocation nucleation in face-centered-cubic and body-centered-cubic bicrystal interfaces, Int. J. Plast. 53 (2014) 40.
[49] J. Hirth, R. Pond, R. Hoagland, et al., Interface defects, reference spaces and the Frank–Bilby equation, Prog. Mater. Sci. 58 (2013) 749.
[50] M.S. . Daw, M.I. Baskes, Embedded-atom method - derivation and application to impurities, surfaces, and other defects in metals, Phys. Rev. B 29 (1984) 6443.
[51] X.Y. Liu, J.B. Adams, F. Ercolessi, et al., EAM potential for magnesium from quantum mechanical forces, Modell. Simul. Mater. Sci. Eng. 4 (1996) 293.
[52] G.J. . Ackland, R. Thetford, An improved N-Body semiempirical model for body-centered cubic transition-metals, Philos. Mag. A 56 (1987) 15.
[53] M.J. . Demkowicz, R.G. Hoagland, Structure of Kurdjumov-Sachs interfaces in simulations of a copper-niobium bilayer, J. Nucl. Mater. 372 (2008) 45.
[54] G. Kresse, J. Furthmuller, Efficiency of ab-initio total energy calculations for

metals and semiconductors using a plane-wave basis set, Comp. Mater. Sci. 6 (1996) 15.
[55] G. Kresse, J. Hafner, Abinitio molecular-dynamics for liquid-metals, Phys. Rev. B 47 (1993) 558.
[56] J.P. Perdew, K. . Burke, M. Ernzerhof, Generalized gradient approximation made simple, Phys. Rev. Lett. 77 (1996) 3865.
[57] P.E. Blochl, Projector augmented-wave method, Phys. Rev. B 50 (1994) 17953.
[58] K. Knowles, The dislocation geometry of interphase boundaries, Philos. Mag. A 46 (1982) 951.
[59] S. Shao, J. Wang, I.J. Beyerlein, et al., Glide dislocation nucleation from dislocation nodes at semi-coherent {1 1 1} Cu–Ni interfaces, Acta Mater. 98 (2015) 206.
[60] S. Shao, J. Wang, A. Misra, Energy minimization mechanisms of semi-coherent interfaces, J. Appl. Phys. 116 (2014) 023508.
[61] S. Shao, J. Wang, A. Misra, et al., Spiral patterns of dislocations at nodes in (111) semi-coherent FCC interfaces, Sci. Rep. 3 (2013) 2448.
[62] I. Salehinia, S. Shao, J. Wang, et al., Interface structure and the inception of plasticity in Nb/NbC nanolayered composites, Acta Mater. 86 (2015) 331.